ACCELERATION STATISTICS IN INHOMOGENEOUS TURBULENT PIPE FLOW USING DIRECT NUMERICAL SIMULATION

Maurice Veenman, Hans Kuerten, Bert Brouwers
Department of Mechanical Engineering,
Technische Universiteit Eindhoven
Den Dolech 2, Eindhoven, 5600 MB, The Netherlands
m.p.b.veenman@tue.nl, j.g.m.kuerten@tue.nl, j.j.h.brouwers@tue.nl

ABSTRACT

One-point acceleration properties are studied for inhomogeneous pipe flow using a direct numerical simulation. The acceleration is decomposed using the Navier-Stokes equations. In general, similar behavior is observed for variances of the acceleration components, probability density functions of the pressure and its gradient, and geometrical alignment as in incompressible, isotropic turbulence (Tsinober *et al.* Phys. Fluids, Vol. 13 (7), 2001). A question which requires further investigation is whether discrepancies from isotropic results are caused by the inhomogeneity of the flow or by the small value of the Re–number.

INTRODUCTION

During the last decade much effort has been spent to describe turbulent transport in a Lagrangian framework. This approach could be of great help to understand for example turbulent dispersion and mixing of passive scalars or contaminants. In the Lagrangian case the time evolution of marked fluid elements (viz. fluid-particles) which follow the motion of the fluid is recorded. This is in contrast with a Eulerian description where the turbulent flow is described at fixed points in space and time. Stochastic models try to simulate this evolution of fluid particles under the assumption that the Reynolds number is high enough so that there is a distinct separation between the smallest scales of the flow and the large, energy containing scales. In this case the fluid particle acceleration can be modeled using a δ-correlated Markov process. Closely related to Lagrangian modelling of dispersion is the material derivative of the velocity vector which, using the Navier-Stokes equations, can be written as

$$\boldsymbol{a} \equiv \frac{D\boldsymbol{u}}{Dt} = \frac{\partial \boldsymbol{u}}{\partial t} + (\boldsymbol{u}\cdot\nabla)\boldsymbol{u} = -\frac{1}{\rho}\nabla p + \nu\nabla^2\boldsymbol{u} \qquad (1)$$

Several physical issues in turbulence based on this decomposition of the acceleration vector have been studied. However, this has only be done for isotropic turbulence. The sum of pressure gradient and the viscous part should equal the sum of the local acceleration and convective acceleration. Using the notation introduced by Tsinober *et al.* (2001), we can also write $\boldsymbol{a} = \boldsymbol{a}_L + \boldsymbol{a}_C = \boldsymbol{a}_I + \boldsymbol{a}_S$, where $\boldsymbol{a}_L \equiv \partial\boldsymbol{u}/\partial t$, $\boldsymbol{a}_C \equiv (\boldsymbol{u}\cdot\nabla)\boldsymbol{u}$, $\boldsymbol{a}_I \equiv -\nabla(p/\rho)$ and $\boldsymbol{a}_S \equiv \nu\nabla^2\boldsymbol{u}$. According to Monin and Yaglom (1975) the total acceleration $\boldsymbol{a}$ is largely dominated by the irrotational pressure gradient and the solenoidal viscous part is small. On the other hand Tennekes' hypothesis assumes that the total acceleration $\boldsymbol{a}$ is small compared to the local and convective accelerations and hence $\boldsymbol{a}_L$ and $\boldsymbol{a}_C$ are strongly negatively correlated. These findings where later confirmed by DNS results of incompressible, forced, isotropic turbulence (Tsinober *et al.*, 2001, Vedula and Yeung, 1999). How all these findings relate to inhomogeneous turbulence is yet unknown. Our primary interest in this article is to investigate the various contributions to the acceleration term obtained from DNS of inhomogeneous pipe flow and to compare the results with those obtained from isotropic turbulence.

The remainder of the article is organized as follows. First, the numerical method and performed calculations are explained. In the subsequent section we will show the DNS results at two different Re–numbers for the various contributions to the total acceleration. Single-point variances and geometric statistics of vector alignment as well as PDF's of the various terms and pressure are shown. Finally, conclusions are summarized.

NUMERICAL METHOD AND GOVERNING EQUATIONS

In this section the numerical method used for DNS of turbulent flow in a cylindrical pipe will be described. In rotational form the continuity and Navier-Stokes equations are given by

$$\nabla\cdot\boldsymbol{u} = 0 \qquad (2)$$

$$\frac{\partial\boldsymbol{u}}{\partial t} + \boldsymbol{\omega}\times\boldsymbol{u} = -\nabla P + \nu\nabla^2\boldsymbol{u} + \boldsymbol{f}, \qquad (3)$$

where $\boldsymbol{u}$ is the velocity vector, P is the total pressure defined as $P = p + \boldsymbol{u}^2/2$, where p is the static pressure, $\boldsymbol{\omega} = \nabla\times\boldsymbol{u}$ is the vorticity vector, $\boldsymbol{f}$ is a forcing term and ν is the kinematic viscosity.

To solve equations (2) and (3) numerically, essentially the same method is used as discussed by Shan *et al.*, 1999. Because of the cylindrical geometry the choice for cylindrical coordinates and cylindrical velocity components is natural. The equations have been non-dimensionalized by the radius of the pipe R, the kinematic viscosity ν and the bulk velocity u_B. The Reynolds number is defined as $Re = u_B D/\nu$ where D is the diameter of the pipe. A finite part of a the pipe of length L is considered using periodic boundary conditions in the axial direction. Combined with the natural periodicity in the tangential direction there are two periodic directions and the choice for a spectral method is obvious. In the radial direction an expansion based on Chebyshev polynomials is used. However, the distribution of the Gauss-Lobatto collocation points leads to very small cells near the pipe axis and thus necessitates the use of very small time steps. Therefore, the radial direction is divided into several elements and in

each element an expansion into Chebyshev polynomials is adopted. At the interfaces between the elements the solution is required to be C^1. Each velocity component and the pressure are thus expanded as:

$$u(r,\phi,z) = \sum_{k_\phi=-a}^{a} \sum_{k_z=-b}^{b} \tilde{u}_{k_\phi,k_z}(r) e^{(ik_\phi\phi + \frac{2\pi}{L} ik_z z)}$$

with $a = M_\phi/2 - 1$ and $b = M_z/2 - 1$, where M_ϕ and M_z are the number of Fourier modes in tangential and axial direction resp. In this way a hybrid method appears: Fourier-Galerkin in the two periodic directions and Chebyshev-collocation in the radial direction. Derivatives in the periodic directions can easily be calculated in spectral space, whereas derivatives with respect to r follow from the Chebyshev derivative matrix (see Canuto *et al.*, 1988). The division of the radial direction into elements makes it possible to reduce the number of Fourier modes in the tangential direction in the element containing the axis of the pipe. This mode reduction does not influence the global accuracy of the method and the corresponding increase in grid size alleviates the time step restriction (see Loulou, 1996).

The Navier-Stokes equations are integrated in time using a time-splitting method by Karniadakis (1991) Schematically the Navier-Stokes equation can be written as

$$\frac{\partial \boldsymbol{u}}{\partial t} + \boldsymbol{N}(\boldsymbol{u}) + \nabla P = \boldsymbol{L}(\boldsymbol{u}) + \boldsymbol{f},$$

where $\boldsymbol{N}$ denotes the nonlinear terms on the left-hand side of (3), $\boldsymbol{L}$ the viscous terms on the right-hand side and $\boldsymbol{f}$ the forcing term. A second-order accurate time-splitting method with constant time step Δt is then given by

$$\left\{ \begin{array}{lcl} \boldsymbol{u}^{n+\frac{1}{3}} & = & 2\boldsymbol{u}^n - \frac{1}{2}\boldsymbol{u}^{n-1} - \Delta t \boldsymbol{f} \\ & & +\Delta t(2\boldsymbol{N}(\boldsymbol{u}^n) - \boldsymbol{N}(\boldsymbol{u}^{n-1})) \\ \Delta P^{n+1} & = & \frac{1}{\Delta t}\nabla \cdot \boldsymbol{u}^{n+\frac{1}{3}} \\ \boldsymbol{u}^{n+\frac{2}{3}} & = & \boldsymbol{u}^{n+\frac{1}{3}} - \Delta t \nabla P^{n+1} \\ \boldsymbol{u}^{n+1} & = & \frac{2}{3}\boldsymbol{u}^{n+\frac{2}{3}} + \frac{2}{3}\Delta t \boldsymbol{L}(\boldsymbol{u}^{n+1}). \end{array} \right. \quad (4)$$

In these formulas the superscript denotes the time level. In the first step the nonlinear terms are treated explicitly. The products of vorticity and velocity are calculated in a pseudo-spectral way, where fast-fourier transforms (FFT) are used to transform from spectral to physical space and back. Aliasing is prevented by the 3/2-rule. This implies that before transforming the solution to physical space extra Fourier modes equal to zero are added in both directions. In each dimension the total number of extra modes is the original number divided by two. After transforming the products back to Fourier space the extra modes are disregarded.

In the second step a Poisson equation for the pressure is solved to ensure that the solution after the third step satisfies the continuity equation. A point that requires special attention in this step is the boundary condition for the pressure at the wall of the pipe. Following Karniadakis (1991) we employ at $r = R$

$$\frac{\partial P^{n+1}}{\partial r} = -\frac{2}{Re}\left(\frac{1}{r}\frac{\partial^2 u_\phi^{n+1}}{\partial r \partial \phi} + \frac{\partial^2 u_z^{n+1}}{\partial r \partial z}\right),$$

where the solution at the new time level is found by linear extrapolation from the solution at the two previous time levels. In order to obtain a unique solution this boundary condition cannot be used for the $(k_\phi, k_z) = (0,0)$ mode. Instead the mean pressure at the wall of the pipe is prescribed. The boundary condition for the pressure at the pipe axis follows from the regularity of the pressure there: $\tilde{P} = 0$ for $k_\phi \neq 0$ and $\partial \tilde{P}/\partial r = 0$ for $k_\phi = 0$.

In the final step the linear, viscous terms in the Navier-Stokes equations are treated implicitly. In cylindrical coordinates the viscous parts of the equations for u_r and u_ϕ are coupled, but they can be decoupled by introducing $u_\pm = u_r \pm i u_\phi$. Moreover, the equations for different Fourier modes are completely decoupled, so that a one-dimensional equation for each Fourier mode and each velocity component results. These one-dimensional problems are solved by a direct method. At the wall of the pipe a no-slip boundary condition is applied. At the pipe axis the boundary conditions follow from the requirement that the Cartesian velocity components are regular. This results in $\tilde{u}_z = 0$ for $k_\phi \neq 0$, $\partial \tilde{u}_z/\partial r = 0$ for $k_\phi = 0$, $\tilde{u}_\pm = 0$ for $k_\phi \neq \mp 1$ and $\partial \tilde{u}_\pm/\partial r = 0$ for $k_\phi = \mp 1$.

Later on, we will present results for Reynolds numbers of 5300 and 10312 based on the bulk velocity and pipe diameter D (or $Re_\tau = 362$ and $Re_\tau = 647$ resp.). For the lower Reynolds number many experimental and numerical results from literature are known (see e.g. Eggels, 1994, Eggels *et al.*, 1994, Loulou, 1996, Wagner, 2001 and Westerweel *et al.*, 1996). The length L of the pipe is taken $L = 10$ which corresponds to $5D$. The number of Chebychev points and Fourier modes used in the simulation are $(109 \times 128 \times 128)$ for resp. the radial, tangential and axial directions for the lower $Re-$number and $(151 \times 256 \times 384)$ for the higher $Re-$number. The largest grid spacings in tangential direction are at the wall due to the cylindrical coordinate system. In the radial direction the largest spacings are close to the center of the pipe to prevent severe limits on the time step as discussed earlier. Table 1 summarizes the grid spacing values expressed in wall units. This grid resolution is comparable with other spectral simulations of wall-bounded flows (Moin and Mahesh, 1998). Temporal correlation functions have been validated with a calculation on a $(172 \times 192 \times 192)$ grid for the lower $Re-$number case. The differences in velocity statistics between the two grids appeared to be negligible.

The calculation is started from a random field superposed on an approximate mean field with the axial velocity component given by a logarithmic velocity profile. The random field is chosen in such a way that it satisfies the continuity equation and that the lowest four Fourier modes in both periodic directions are unequal to zero. In the first time step, scheme (4) cannot be applied since only one field is available. A first-order time-splitting scheme is used instead. After a large number of time steps a state of fully-developed turbulence is reached. From that time onwards averaged flow quantities can be calculated. The two simulations ($Re_\tau = 362$ and $Re_\tau = 647$) are run for $20t^*$, where $t^* = D/u_*$, with fixed time steps $\Delta t = 2.0 \times 10^{-4}$ and $\Delta t = 1.0 \times 10^{-4}$ resp., which leads to more than 100 statistically independent fields for both cases. Averaging is performed over the periodic directions and time. The code has been tested thoroughly by comparing statistical quantities like r.m.s. profiles of velocity-, vorticity- and pressure-fluctuations, spatial and temporal correlation functions, spatial velocity spectra and the budgets of the turbulent kinetic energy equation with experimental and numerical data of others. A comparison of most of these statistics with available results from others can be found in Kuerten *et al.* (2001).

SINGLE-POINT VARIANCES

In this section we study the components of the one-point

Table 1: Grid spacing expressed in wall units. Re_τ is based on the friction velocity u_τ: $Re_\tau = u_\tau D/\nu$

Re_τ	Δr^+_{min}	Δr^+_{max}	$R\Delta\phi^+_{max}$	Δz^+	$\eta^+ \approx$
362	0.11	4.03	8.89	14.10	1.58
647	0.09	4.47	7.95	8.43	1.49

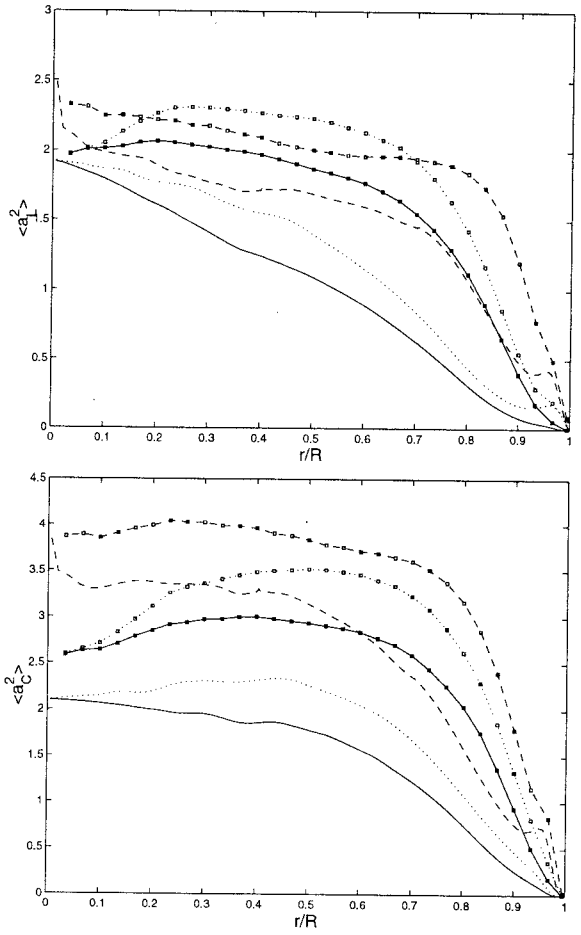

Figure 1: Acceleration variances normalized by $\langle\epsilon\rangle^{3/2}\nu^{-1/2}$ as function of the radius. Solid: radial component, dotted: tangential component, dashed: axial component. Lines without and with the markers are at $Re_\tau = 362$ and $Re_\tau = 647$ resp.

acceleration variance scaled with Kolmogorov variables. In isotropic, homogeneous turbulence statistical properties of variables of interest can be obtained by averaging over time and the complete computational domain. In inhomogeneous pipe flow all statistical properties depend on the radius. A problem that arises here is the definition of the $Re-$number which will be addressed later. For now we will present all results as function of the radius when appropriate. Since there is a large mean flow the local and convective acceleration strongly dominate over the pressure gradient and viscous term. Hence the mean flow contributions are subtracted from the acceleration terms. Figures 1 and 2 show ensemble averaged results for $\langle \boldsymbol{a}_L^2 \rangle$, $\langle \boldsymbol{a}_C^2 \rangle$, $\langle \boldsymbol{a}_I^2 \rangle$ and $\langle \boldsymbol{a}_S^2 \rangle$. Since we are dealing with inhomogeneous flow the result is plotted for every individual velocity component. For a more quantified comparison Table 2 and Table 3 show the ratios

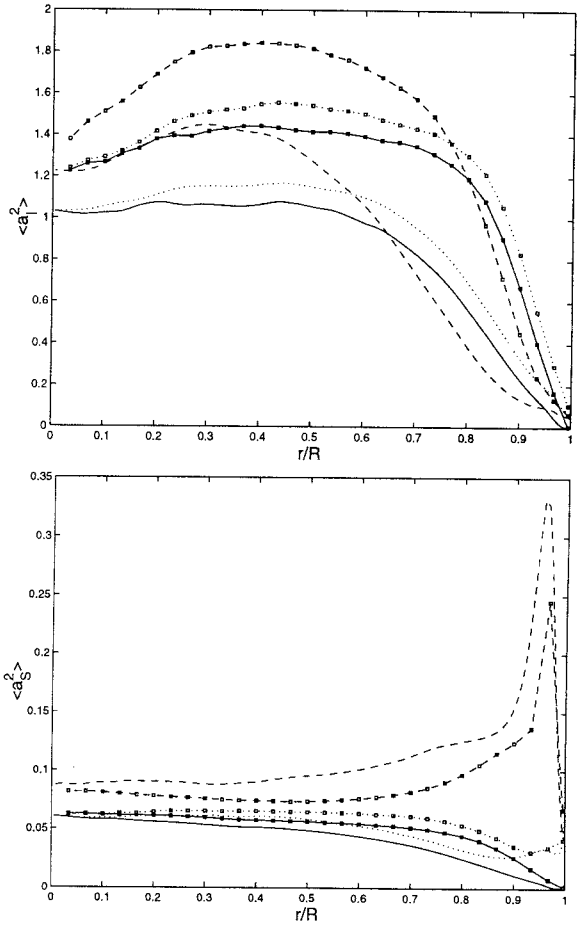

Figure 2: Acceleration variance normalized by $\langle\epsilon\rangle^{3/2}\nu^{-1/2}$ as function of the radius. Solid: radial component, dotted: tangential component, dashed: axial component. Lines without and with the markers are at $Re_\tau = 362$ and $Re_\tau = 647$ resp.

between the components at a radial position of $r/R = 0.5$ for $Re_\tau = 362$ and $Re_\tau = 647$ resp. Several aspects also observed for isotropic turbulence (Tsinober *et al.*, 2001, Vedula and Yeung, 1999) can be observed. According to Tennekes' hypotheses the total acceleration $\boldsymbol{a}$ should be small compared to its local and convective contributions ($\boldsymbol{a}_L$ and $\boldsymbol{a}_C$), which on their turn should have variances close to each other. The total acceleration should also be close to the contribution from the pressure gradient. The values for $\langle \boldsymbol{a}^2 \rangle$ are not shown in the figure, but results from Tables 2 and 3 indeed indicate that $\langle a \rangle \approx \langle a_I \rangle$. Tsinober *et al.* (2001) remarked that since $\boldsymbol{a}_I$, which is irrotational, dominates over $\boldsymbol{a}_S$, $\boldsymbol{a}$ should be nearly irrotational as well. On the other hand $\boldsymbol{a}_L$ is solenoidal. In homogeneous turbulence irrotational and solenoidal vectors are uncorrelated. They indeed find no correlation between $\boldsymbol{a}$ and $\boldsymbol{a}_L$, even at very small values for Taylor Reynolds number Re_λ ($Re_\lambda = u_{rms}\lambda/\nu$, where λ is the Taylor length scale). Our results clearly show that $\boldsymbol{a}$ and $\boldsymbol{a}_L$ are no longer completely uncorrelated, due to inhomogeneity. Since $\boldsymbol{a} = \boldsymbol{a}_L + \boldsymbol{a}_C$ and $\boldsymbol{a}$ is small, $\boldsymbol{a}_C$ and $\boldsymbol{a}_L$ must cancel each other, i.e. they should be negatively correlated. The correlation coefficient $\rho(\boldsymbol{a}_L, \boldsymbol{a}_C)$ shown in Tables 2 and 3 show a slight decrease towards -1 for the radial and tangential component, but opposite behavior for the axial component. Whether or not this is a low Reynolds

number effect is unclear at this moment. This opposite behavior of the axial component is also observed in Figure 2 for $\boldsymbol{a}_S$. The numerical values of around -0.7 for $\rho(\boldsymbol{a}_L, \boldsymbol{a}_C)$ are relatively far from the values found by Tsinober *et al.* (2001). They find a value of approx. -0.9 at their highest Reynolds number.

Table 2: Ratios of variances of acceleration components and correlation coefficients. The results are for a radial position of $r/R = 0.5$ and at a $Re-$number of $Re_\tau = 362$.

	r	ϕ	z
$\langle a^2 \rangle / \langle a_L^2 \rangle$	0.9845	0.8585	0.8380
$\langle a^2 \rangle / \langle a_C^2 \rangle$	0.6011	0.5274	0.4510
$\langle a_L^2 \rangle / \langle a_C^2 \rangle$	0.6106	0.6143	0.5381
$\rho(a, a_L)$	0.1747	0.1245	-0.0111
$\rho(a, a_C)$	0.6388	0.6287	0.6797
$\rho(a_L, a_C)$	-0.6460	-0.6934	-0.7410
$\langle a^2 \rangle / \langle a_I^2 \rangle$	1.0125	1.0365	1.1127
$\langle a^2 \rangle / \langle a_S^2 \rangle$	22.0145	20.5903	14.8064
$\langle a_I^2 \rangle / \langle a_S^2 \rangle$	21.7420	19.8657	13.3063
$\rho(a, a_I)$	0.9772	0.9754	0.9658
$\rho(a, a_S)$	0.1356	0.1900	0.3249

Table 3: Same as Table 2 for $Re_\tau = 647$.

	r	ϕ	z
$\langle a^2 \rangle / \langle a_L^2 \rangle$	0.7736	0.7165	0.9588
$\langle a^2 \rangle / \langle a_C^2 \rangle$	0.4924	0.4539	0.5012
$\langle a_L^2 \rangle / \langle a_C^2 \rangle$	0.6365	0.6334	0.5227
$\rho(a, a_L)$	0.1152	0.0814	0.0234
$\rho(a, a_C)$	0.6098	0.6089	0.6910
$\rho(a_L, a_C)$	-0.7170	-0.7410	-0.7064
$\langle a^2 \rangle / \langle a_I^2 \rangle$	1.0208	1.0363	1.0592
$\langle a^2 \rangle / \langle a_S^2 \rangle$	25.7896	24.8437	26.2856
$\langle a_I^2 \rangle / \langle a_S^2 \rangle$	25.2650	23.9732	24.8159
$\rho(a, a_I)$	0.9805	0.9797	0.9808
$\rho(a, a_S)$	0.1501	0.1876	0.2409

GEOMETRICAL STATISTICAL PROPERTIES

In line with Tsinober *et al.* (2001) we will discuss here alignment properties of $\boldsymbol{a}$, $\boldsymbol{a}_L$ and $\boldsymbol{a}_C$ and alternatively $\boldsymbol{a}$, $\boldsymbol{a}_I$ and $\boldsymbol{a}_S$ relative to each other. The notation $\theta(\mathbf{V}_1, \mathbf{V}_2)$ is used for the angle between any two vectors $\mathbf{V}_1$ and $\mathbf{V}_2$. Due to the dependence of statistics on the radius we will restrict ourselves to one single radial position when convenient. The cancellation between local and convective acceleration indicates that these two vectors should be antiparallel, i.e. the angle should be close to 180 degrees. This was already confirmed by Tsinober *et al.* (2001) for isotropic turbulence. In Figure 3 PDF's for $\theta(\mathbf{a}_L, \mathbf{a}_C)$ (a) and also $\theta(\mathbf{a}, \mathbf{a}_C)$ and $\theta(\mathbf{a}, \mathbf{a}_L)$ (b) are shown for the two $Re-$numbers at $r/R = 0.5$. The same is repeated in Figure 4 for the PDF's for $\theta(\mathbf{a}_I, \mathbf{a}_S)$ (a) and also $\theta(\mathbf{a}, \mathbf{a}_I)$ and $\theta(\mathbf{a}, \mathbf{a}_S)$ (b). There is indeed a large peak of the PDF of $\theta(\mathbf{a}_L, \mathbf{a}_C)$ close to 180^o. Although not as clear as in Tsinober's simulations there is a tendency for the angle to get more antiparallel with increasing $Re-$number. Tsinober *et al.* (2001) simulated almost an order of magnitude in the Taylor $Re-$number ranging from

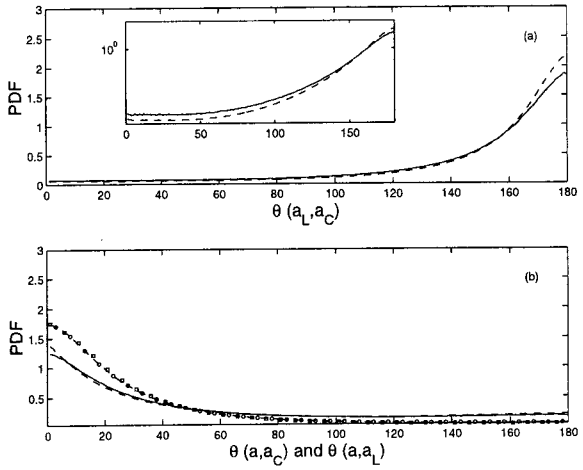

Figure 3: (a) PDF's of $\theta(\mathbf{a}_L, \mathbf{a}_C)$ in degrees at $Re_\tau = 362$ and $Re_\tau = 647$ (solid and dashed resp.). The smaller figure is the same but with a logarithmic scale. Figures are comparable with Tsinober *et al.* (2001). (b) PDF's of $\theta(\mathbf{a}, \mathbf{a}_C)$ (lines incl. markers) and $\theta(\mathbf{a}, \mathbf{a}_L)$ (lines without markers) at $Re_\tau = 362$ (solid) and $Re_\tau = 647$ (dashed).

$Re_\lambda = 38$ to $Re_\lambda = 243$. In our simulations there is merely a factor 1.9 in $Re-$number range. The trend with $Re-$number is also not very clear in Figure 5 where the mean values of the cosines of the angles between $\boldsymbol{a}$, $\boldsymbol{a}_L$ and $\boldsymbol{a}_C$ and $\boldsymbol{a}$, $\boldsymbol{a}_I$ and $\boldsymbol{a}_S$ as function of the radius is given. The anti-alignment between $\boldsymbol{a}_L$ and $\boldsymbol{a}_C$ does slightly increase to approx. -0.6, but is still far from Tsinober's values of around -0.8 at their highest $Re_\lambda-$number of 243. Figure 5 also shows that all angles exhibit a constant, or nearly constant, behavior over a large range of the radial coordinate. Only in the near-wall region, there is deviation from constant behavior. Here, $cos(\boldsymbol{a}, \boldsymbol{a}_I)$, $cos(\boldsymbol{a}, \boldsymbol{a}_C)$, $cos(\boldsymbol{a}, \boldsymbol{a}_s)$ and $cos(\boldsymbol{a}_C, \boldsymbol{a}_I)$ all go to zero. Near the wall all components of the velocity tend to zero. However, as the convective terms scale with $\boldsymbol{u}^2$, they tend to zero faster than the local acceleration. Hence, close to the wall the total acceleration is dominated by local acceleration and $cos(\boldsymbol{a}, \boldsymbol{a}_L)$ goes to unity. On the other hand $\boldsymbol{a} = \boldsymbol{a}_I + \boldsymbol{a}_S$ and $\boldsymbol{a}_S$ is unequal to zero at the wall, since $\partial^2 \boldsymbol{u}/\partial r^2 \neq 0$. This implies that the pressure gradient is unequal to zero as well and $cos(\boldsymbol{a}_I, \boldsymbol{a}_S) \rightarrow -1$.

Figure $3^{(b)}$ shows that $\boldsymbol{a}$ is positively aligned with $\boldsymbol{a}_L$ and $\boldsymbol{a}_C$. There is hardly any $Re-$number dependence for both $\theta(\mathbf{a}, \mathbf{a}_C)$ and $\theta(\mathbf{a}, \mathbf{a}_L)$. However, this is probably due to the slight increase in $Re-$number since Tsinober *et al.* (2001) found that the alignment of $\boldsymbol{a}$ and $\boldsymbol{a}_C$ decreases significantly at higher $Re-$number. In agreement with their results is the lack of $Re-$number dependence for the alignment of $\boldsymbol{a}$ with $\boldsymbol{a}_L$. They find a nearly constant mean angle between the vectors $\boldsymbol{a}$ and $\boldsymbol{a}_L$ over the whole $Re-$number range of approx. 0.1. Our results give a constant, but much higher value of approx. 0.25. This is easily seen in Figure 5.

In Figure 4 similar information is shown as in Figure 3, but for the vectors $\boldsymbol{a}$, $\boldsymbol{a}_I$ and $\boldsymbol{a}_S$. The outcome is comparable with results for isotropic turbulence. The PDF of $\theta(\mathbf{a}_I, \mathbf{a}_S)$ is relatively flat, meaning that there is no preferential alignment between these two vectors, and has no $Re-$number dependence. Since $\langle a \rangle \approx \langle a_I \rangle$ it is expected that $\boldsymbol{a}$ is almost aligned with $\boldsymbol{a}_I$ and less so with $\boldsymbol{a}_S$. This is illustrated in Figure $4^{(b)}$ and in agreement with Tsinober *et al.* (2001).

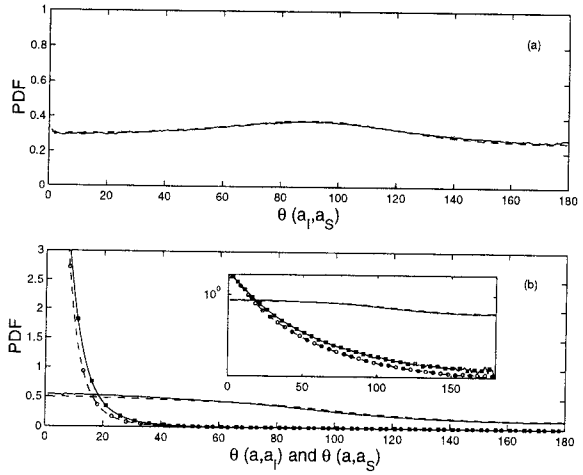

Figure 4: (a) PDF's of $\theta(\mathbf{a}_I, \mathbf{a}_S)$ in degrees at $Re_\tau = 362$ and $Re_\tau = 647$ (solid and dashed resp.). (b) PDF's of $\theta(\mathbf{a}, \mathbf{a}_I)$ (lines incl. markers) and $\theta(\mathbf{a}, \mathbf{a}_S)$ (lines without markers) at $Re_\tau = 362$ (solid) and $Re_\tau = 647$ (dashed). The smaller figure is the same but with a logarithmic scale.

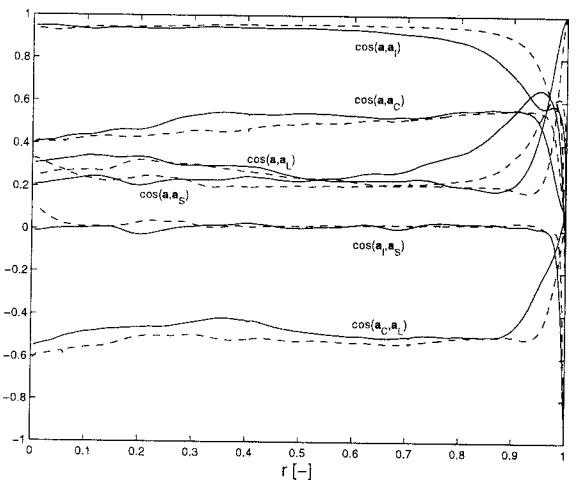

Figure 5: Mean values of the cosines of the angles between $\boldsymbol{a}$, $\boldsymbol{a}_L$ and $\boldsymbol{a}_C$ and $\boldsymbol{a}$, $\boldsymbol{a}_I$ and $\boldsymbol{a}_S$ as function of the radius.

PROBABILITY DENSITY FOR PRESSURE

The standardized, i.e. scaled with its variance, one-point pressure PDF is shown in Figure 6. The plot is in a semi-logarithmic scaling to observe the behavior in the tails. The solid line represents the result at the lowest $Re-$number and the dotted line is the result at the higher $Re-$number. Both results are at a position $r/R = 0.5$. Figure 7 essentially shows the same results, but now only for the higher $Re-$number at three radial positions. The pressure PDF is negatively skewed (Cadot *et al.*, 1994). For isotropic turbulence the shape of the PDF for positive fluctuations is close to the Gaussian distribution. Vedula and Yeung (1999) suggest that this part could also be described by exponential decay. That would mean in this semi-logarithmic plot that this part follows a straight line. In our case, however, the shape of the PDF for positive fluctuations clearly deviates from Gaussian or exponential behavior. Also Cadot *et al.* (1994), who performed experiments in a closed, stirred cylindrical box, found a perfect Gaussian fit for positive pressure. However, this was only observed for sufficiently high

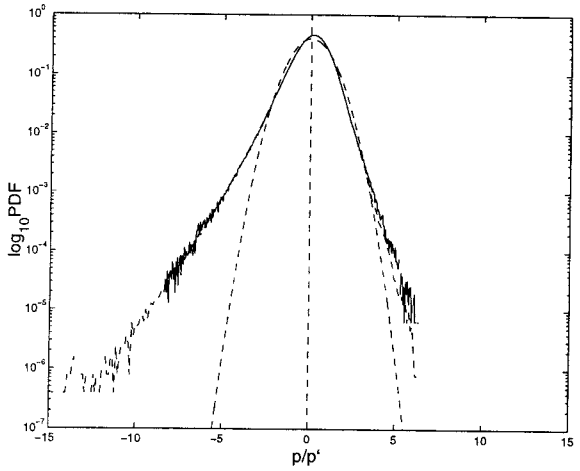

Figure 6: Base-10 logarithm of the standardized pressure fluctuation PDF. Results are shown for $r/R = 0.5$. The solid line is for $Re_\tau = 362$ and the dashed line is for $Re_\tau = 647$. The smooth dashed line represents a Gaussian distribution.

$Re-$numbers. At lower $Re-$numbers they also find deviations from Gaussian behavior. In regions close to the wall ($r/R > 0.9$), the PDF starts to deviate from the PDF of more inner regions as can be observed in Figure 7.

The shape of the PDF for negative fluctuations shows no $Re-$number dependence. Vedula and Yeung (1999) find universal behavior for this part of the PDF. Furthermore, they find exponential tails (i.e. straight lines) up to $p/p' \approx -10$ for all $Re-$numbers. At around $p/p' \approx -13$ the tail changes shape by stretching more outwards. Our $Re-$number range is too small to observe whether or not this phenomenon also takes place for pipe flow, but an exponential decay is not observed for the region $-10 < p/p' < 0$.

The standardized PDF of the pressure gradient is shown in Figure 8. Here, results for both $Re_\tau = 362$ and $Re_\tau = 647$ are included. To distinguish between the various components, we use circles for $\partial p/\partial r$, squares for $\partial p/\partial \phi$ and diamonds for $\partial p/\partial z$. The figure shown is at a radial position of $r/R = 0.5$. There are small differences between the three separate components. These differences become bigger in the region $r/R > 0.9$ (not shown here). There seems to be no or very little $Re-$number dependence. This is in contradiction with Vedula and Yeung (1999). As the Reynolds number increases, their PDF stretches out towards larger magnitudes of ∇p. This is already observed are relatively low Reynolds numbers.

SUMMARY AND CONCLUDING REMARKS

The various acceleration components in the Navier-Stokes equations have been analyzed for inhomogeneous pipe flow. Although there are many similarities with isotropic turbulence, some differences can be observed as well. In view of Reynolds number dependence we now studied results at two different Reynolds numbers based on the bulk velocity by looking at the same radial position for both cases. One might argue that this is not correct and we should compare results based on local Reynolds numbers, i.e. depending on the radial position. The problem of defining such a Reynolds number, as mentioned earlier, limits the possibility to collapse all results for various components of the acceleration. Since there is a dependence of statistics on the radial position, the local Reynolds number should depend on the radial

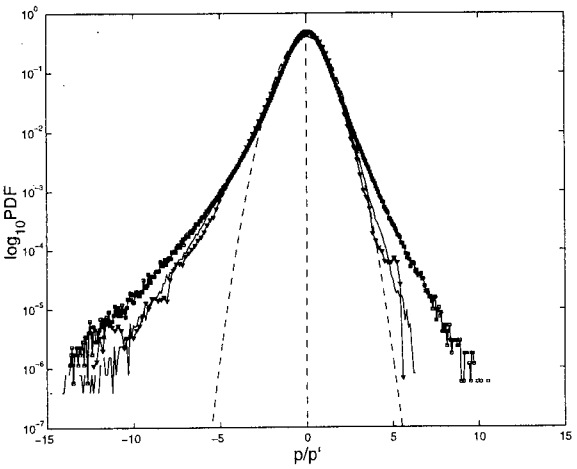

Figure 7: Base-10 logarithm of the standardized pressure fluctuation PDF, but now only results for $Re_\tau = 647$ at various radial positions are shown. Triangle: $r = 0.1$, solid: $r = 0.5$, squares: $r = 0.95$.

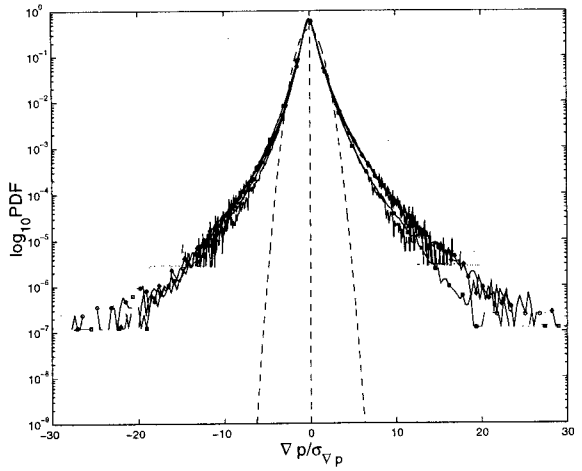

Figure 8: Same as Figure 6 but for the pressure gradient. Each component of the pressure gradient is studied separately. Result are shown for both $Re_\tau = 362$ and $Re_\tau = 647$ (longer, extended lines). Circles: radial component, squares: tangential component, diamonds: axial component. Results are for $r/R = 0.5$.

position as well. Hill (2002) suggested not to use Re_λ to scale the results, since it is based on u_{rms} and hence not universal. Instead he defined a new $Re-$number, R_a, as the ratio between $\langle a \rangle^{1/2}$ and $\langle a_S \rangle^{1/2}$, i.e. total (or fluid-particle) and viscous acceleration. This scaling did not give satisfying results in our case.

A question which requires further investigation is whether discrepancies from isotropic results by Tsinober *et al.* (2001) are caused by the inhomogeneity of the flow or by the small value of the $Re-$number. To investigate this, simulations at higher $Re-$number should be performed.

ACKNOWLEDGMENTS

This work was sponsored by the Stichting Nationale Computerfaciliteiten (National Computing Facilities Foundation, NCF) for the use of supercomputer facilities, with financial support from the Nederlandse Organisatie voor Wetenschappelijk Onderzoek (Netherlands Organization for Scientific Research, NWO).

REFERENCES

Cadot A., Douady S. and Couder, Y., 1994, "Characterization of the Low-Pressure Filaments in a Three-Dimensional Turbulent Shear Flow", *Phys. Fluids*, Vol. 7 (3), pp. 630-646.

Canuto C., Hussaini M.Y., Quarteroni A. and Zang T.A., 1988, "Spectral Methods in Fluid Dynamics", Springer-Verlag, Berlin.

Eggels J.G.M., 1994, "Direct and Large Eddy Simulation of Turbulent Flow in a Cylindrical Pipe Geometry", Ph.D. Thesis, Delft University of Technology, Department of Aero- and Hydrodynamics.

Eggels J.G.M., Unger F., Weiss M.H., Westerweel J., Adrian R.J., Friedrich R., Nieuwstadt F.T.M., 1994, "Fully Developed Turbulent Pipe Flow: a Comparison Between Direct Numerical Simulation and Experiment", *J. Fluid Mech.*, Vol. 268, pp. 175-209.

Hill R.J., 2002, "Possible Alternative to R_λ-scaling of Small-Scale Turbulence Statistics", *J. Fluid Mech.*, Vol. 463, pp. 403-412.

Karniadakis G.E., Israeli M. and Orszag S.A., 1991, "High-order splitting methods for the incompressible Navier-Stokes equations", *J. Comp. Phys.*, Vol. 97, pp. 414-443.

Kuerten J.G.M., Veenman M.P.B. and Brouwers J.J.H., 2001, "Simulation of the Motion of Particles in Turbulent Flow", in B.J. Geurts, R. Friedrich. and O. Métais, eds., *Direct and Large-Eddy Simulation IV, 2001*, Enschede, pp. 11-20.

Loulou P., 1996, "Direct Numerical Simulation of Incompressible Pipe Flow Using a B-Spline Spectral Method", Ph.D. Thesis, Stanford University, Department of Aeronautics and Astronautics.

Moin P. and Mahesh K., 1998, "Direct Numerical Simulation: A Tool in Turbulence Research", *Annu. Rev. Fluid Mech.*, Vol. 30, pp. 539-578.

Monin A.S., Yaglom A.M., 1975, "Statistical Fluid Mechanics", Vol. 2, M.I.T. Press, Cambridge.

Shan H., Ma B., Zhang Z. and Nieuwstadt F.T.M., 1999, "Direct Numerical Simulation of a Puff and a Slug in Transitional Cylindrical Pipe Flow", *J. Fluid Mech.*, Vol. 387, pp. 39-60.

Tennekes H., 1975, "Eulerian and Lagrangian Time Microscales in Isotropic Turbulence", *J. Fluid Mech.*, Vol. 67, pp. 561-567.

Tsinober A., Vedula P. and Yeung, P.K., 2001, "Random Taylor Hypothesis and the Behavior of Local and Convective Accelerations in Isotropic Turbulence", *Phys. Fluids*, Vol. 13 (7), pp. 1974-1984.

Vedula P. and Yeung, P.K., 1999, "Similarity Scaling of Acceleration and Pressure Statistics in Numerical Simulations of Isotropic Turbulence", *Phys. Fluids*, Vol. 11 (5), pp. 1208-1220.

Wagner C., Hüttl T.J., Friedrich R., 2001, "Low-Reynolds-Number Effects Derived from Direct Numerical Simulations of Turbulent Pipe Flow", *Computers & Fluids*, Vol. 30, pp. 581-590.

Westerweel J., Draad A.A., Hoeven van der J.G.Th, Oord van J., 1996, "Measurement of Fully-Developed Turbulent Pipe Flow With Digital Particle Image Velocimetry", *Exp. in Fluids*, Vol. 20, pp. 165-177.